Joule

Article

Dual-pseudohalide engineering suppresses halide segregation in wide-band-gap perovskites

Graphical abstract

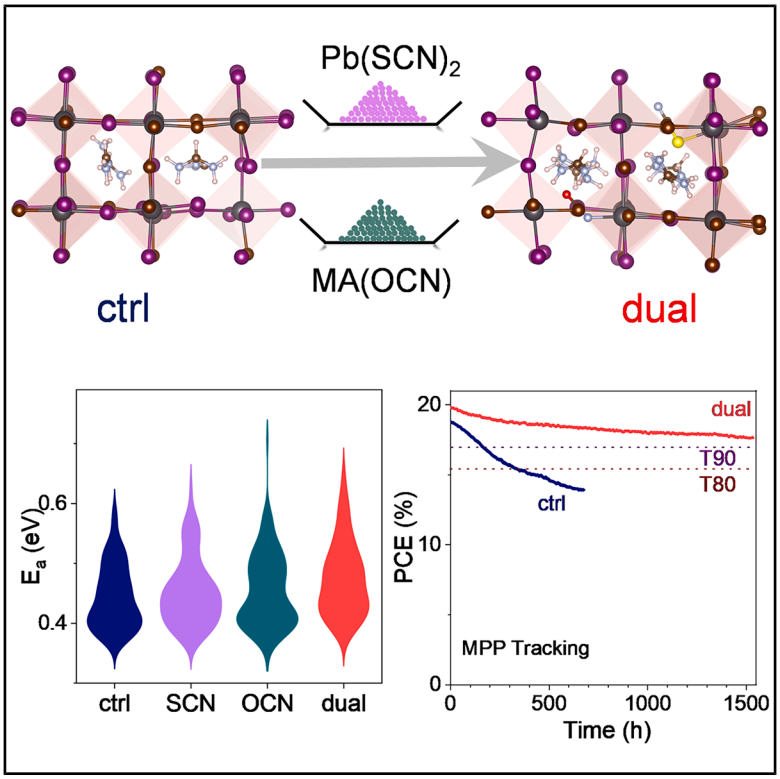

Highlights

- Dual SCN^-/OCN^- alloying suppresses halide vacancies and increases ion migration barriers
- Dual pseudohalides reduce ionic conductivity 5-fold and delay phase segregation 10-fold
- 1.78-eV cells retain 90% of initial PCE after 1,530 h of continuous illumination at 65°C
- All-perovskite tandems achieve 27.2% efficiency with improved stability

Authors

Pronoy Nandi, Chiung-Han Chen, Vikram, ..., Bin Chen, Edward H. Sargent, Mercouri G. Kanatzidis

Correspondence

saiful.islam@materials.ox.ac.uk (M.S.I.), bin.chen@northwestern.edu (B.C.), ted.sargent@northwestern.edu (E.H.S.), m-kanatzidis@northwestern.edu (M.G.K.)

In brief

Light-induced halide segregation remains the principal stability bottleneck in mixed-halide wide-band-gap perovskites. Here, dual SCN^-/OCN^- alloying induces an emergent cooperative frustration within the halide sublattice, creating a non-additive distortion field that simultaneously suppresses halide vacancy formation and elevates ion migration barriers. This cooperative mechanism delays phase segregation by an order of magnitude while preserving optoelectronic quality, providing a general design principle for stable wide-band-gap absorbers in tandem photovoltaics.

Nandi et al., 2027, Joule *11*, 102669
March 17, 2027
https://doi.org/10.1016/j.joule.2026.102669

CellPress

Please cite this article in press as: Nandi et al., Dual-pseudohalide engineering suppresses halide segregation in wide-band-gap perovskites, Joule (2026), https://doi.org/10.1016/j.joule.2026.102669

Joule

CellPress

Article

Dual-pseudohalide engineering suppresses halide segregation in wide-band-gap perovskites

Pronoy Nandi,[1,5] Chiung-Han Chen,[1] Vikram,[2] Cheng Liu,[1] Yurui Wang,[1] Alekos Jackson,[2] Levi Hoogendoorn,[3] Shreyash S. Hadke,[3] Mark C. Hersam,[1,3,4] M. Saiful Islam,[2,*] Bin Chen,[1,4,*] Edward H. Sargent,[1,4,*] and Mercouri G. Kanatzidis[1,6,*]

[1]Department of Chemistry, Northwestern University, Evanston, IL 60208, USA
[2]Department of Materials, University of Oxford, Oxford OX1 3PH, UK
[3]Department of Materials Science and Engineering, Northwestern University, Evanston, IL 60208, USA
[4]Department of Electrical and Computer Engineering, Northwestern University, Evanston, IL 60208, USA
[5]Present address: Center for Sustainable Energy, Indian Institute of Technology Roorkee, Roorkee 247667, India
[6]Lead contact
*Correspondence: saiful.islam@materials.ox.ac.uk (M.S.I.), bin.chen@northwestern.edu (B.C.), ted.sargent@northwestern.edu (E.H.S.), m-kanatzidis@northwestern.edu (M.G.K.)
https://doi.org/10.1016/j.joule.2026.102669

CONTEXT & SCALE Mixed-halide wide-band-gap perovskites are essential for achieving high-efficiency all-perovskite tandem solar cells. However, their long-term stability is limited by light-induced halide segregation, which is closely associated with vacancy-mediated halide migration. Most existing strategies focus either on reducing defect densities or controlling lattice strain, while simultaneously suppressing vacancy formation and hindering ion migration remains challenging. Here, we introduce dual-pseudohalide alloying with thiocyanate (SCN^-) and cyanate (OCN^-) to simultaneously suppress vacancy formation and hinder ion migration. Their incorporation into the halide sublattice induces local lattice distortions, increasing the energetic barrier to halide migration. This strategy reduces ionic conductivity 5-fold and delays phase segregation 10-fold under accelerated illumination.

SUMMARY

Mixed-halide wide-band-gap perovskites are essential for high-efficiency tandem photovoltaics, yet light-induced halide segregation limits their operational stability. To address this, we demonstrate that incorporating bulky pseudohalide anions suppresses vacancy formation and inhibits ion migration pathways. Being large, triatomic anions, thiocyanate (SCN^-) and cyanate (OCN^-) locally distort the perovskite crystal structure, effectively "stuffing" the lattice. This co-doping strategy elevates the ion migration barrier and leads to a 5-fold suppression of ionic conductivity and a 10-fold delay in phase segregation under 10-sun illumination. Wide-band-gap (1.78 eV) solar cells based on this alloy deliver 20% efficiency, with 90% retention after 1,530 h of continuous operation at 65°C, placing it among the most stable wide-band-gap perovskites reported at this temperature. When integrated into all-perovskite tandems, they achieve 27.2% efficiency and retain 70% of their initial efficiency after 600 h at 65°C.

INTRODUCTION

Single-junction solar cells suffer energy losses due to the mismatch between the solar spectrum and a fixed band gap, causing high-energy photons to lose excess energy as heat and low-energy photons to pass through unabsorbed. All-perovskite tandem solar cells, combining wide-band-gap (~1.78 eV) and narrow-band-gap (~1.25 eV) perovskites, address this limitation by capturing a broader spectrum, surpassing single-junction efficiencies (30.1% vs. 27.0%), although long-term stability remains a key challenge for commercialization.[1–6]

However, wide-band-gap perovskites of the type $APbX_3$ (where A = FA, Cs; and $X = I_{1-y}Br_y$), which are typically bromide-rich, suffer from intrinsic instability originating from their soft lattice structure and rapid crystallization kinetics. These features facilitate the formation of point defects, particularly vacancies that promote halide ion migration.[7–9] Under illumination, such ion migration triggers light-induced halide segregation (LIHS),[10–12] where the material phase separates into iodide-rich and bromide-rich domains, leading to reduced open-circuit voltage (V_{OC}) and shorter carrier lifetimes.[13–17] The driving forces behind LIHS are multifaceted: photoinduced thermodynamic

Please cite this article in press as: Nandi et al., Dual-pseudohalide engineering suppresses halide segregation in wide-band-gap perovskites, Joule (2026), https://doi.org/10.1016/j.joule.2026.102669

forces,[18–20] polaron-induced strain,[14,21] and partial lattice self-healing processes involving recombination of halide vacancies and interstitials.[22,23] Moreover, the low formation energies of halide vacancies, especially iodide ($V_I\cdot$) and bromide ($V_{Br}\cdot$), further accelerate this process by increasing defect density and enhancing halide diffusivity.[24] These accumulated defects not only degrade the optoelectronic performance of wide-band-gap perovskites but also disrupt charge transport across the interconnecting layer,[25] ultimately compromising both the efficiency and long-term durability of all-perovskite tandem solar cells.

To address LIHS in wide-band-gap perovskites, strategies have been adopted that include solvent engineering, nanoscale morphology control, quantum dot integration, mixed cation/halide systems, and inclusion of functional additives. These enhance crystallinity, reduce vacancy formation, and limit ion migration.[26–28] Pseudohalide additives, such as thiocyanate (SCN^-),[17] hexafluorophosphate (PF_6^-),[29] tetrafluoroborate (BF_4^-),[30] and tetrahydroborate (BH_4^-)[31] have garnered particular attention due to their comparable ionic radii to halides and efficacy in controlling the crystallization kinetics, thereby reducing the formation of halide vacancies. These approaches primarily raise the formation energy of new vacancies and reduce trap-assisted recombination; however, they leave the connectivity and topology of the halide migration network largely unaltered, resulting in only moderate improvement to ion migration barriers.

Partial substitution of halides with SCN^- or its structural analog, cyanate (OCN^-), has been shown to preferentially occupy iodide vacancy sites ($V_i\cdot$), forming randomly mixed I/Br/SCN(OCN) alloys.[17,32] This substitution induces lattice contraction, widens the band gap, improves crystal orientation, and elevates vacancy formation energies. Nevertheless, when introduced singly and at low concentrations, these pseudohalides only modestly perturb the linear Pb–X–Pb connectivity, limiting their impact on octahedral distortion and halide migration barriers.[33] Excess loading further leads to dual-phase formation, underscoring the narrow compositional window accessible for single-pseudohalide incorporation. In contrast, efforts to increase ion migration barriers have relied on A-site alloying or strain engineering to distort the lattice through octahedral tilts, tuning the tolerance factor.[16,34] These approaches increase migration barriers but do not modify the halide sublattice chemistry, where defects originate and migrate. Critically, A-site-induced distortion and X-site passivation operate on different sublattices and are optimized under separate, often competing, constraints such as phase stability, band gap, and carrier mobility. As a result, their effects are not linearly additive, and concurrent optimization often results in significant trade-offs.

Motivated by this disconnect, we sought to unify defect passivation and lattice distortion within a single sublattice by encoding both effects directly at the X-site. To test this hypothesis, we implemented a dual-pseudohalide co-alloying strategy in which SCN^- and OCN^- are simultaneously incorporated into a wide-band-gap perovskite (Figure 1A). Both pseudohalides adopt bent, bridging configurations between neighboring Pb^{2+} centers, contrasting the linear Pb–X–Pb linkages of halides and inducing pronounced local distortions (Figures 1B–1D). Their complementary bonding chemistries—the π-delocalized, covalent S-C-N backbone of SCN^- and the compact, more electronegative C–O linkage of OCN^-—generate distinct Pb-additive-Pb coordination environments and heterogeneous lattice distortions. This broader distribution of locally distorted migration environments raises the barrier for iodide migration, while pseudohalide incorporation also reduces the equilibrium vacancy population relative to the undoped control, thereby suppressing halide redistribution and phase segregation. The resulting SCN/OCN co-alloyed wide-band-gap perovskites enable single-junction devices with 20% efficiency and retain 90% of their initial performance after 1,530 h at 65°C, one of the best stabilities for this band gap (Figure 1E). The corresponding tandem devices deliver 27.2% efficiency with comparable operational durability at 65°C, demonstrating that emergent cooperative frustration provides a new mechanistic pathway to overcome the intrinsic instability of mixed-halide perovskites and advance stable all-perovskite tandem photovoltaics.

RESULTS AND DISCUSSION

Dual-pseudohalide doping into the perovskite lattice

To realize our strategy, SCN^- and OCN^- anions were incorporated into the $Cs_{0.2}FA_{0.8}Pb(I_{0.63}Br_{0.37})_3$ lattice by doping the perovskite precursor solutions with $Pb(SCN)_2$ and MAOCN, respectively. Based on previous reports, $Pb(SCN)_2$ is known to undergo a reaction with FAI during thermal annealing, yielding PbI_2, thiocyanic acid (HSCN), and volatile formamidine gas.[17,35] Our preliminary tests indicate that all precursor solutions remained uniformly transparent with a light-yellow hue, indicating no visible changes in solubility or precursor stability upon pseudohalide addition. X-ray diffraction (XRD) measurements (Figure S1) revealed a progressive shift of diffraction peaks toward higher 2θ values with increasing pseudohalide concentration, indicative of lattice contraction (unit cell volume reduced from 235.8 to 228.1 $Å^3$) and successful incorporation of pseudohalide anions into the perovskite framework (Figures 2A and 2B).[17,32] OCN^--doped films exhibited a more pronounced shift than those doped with SCN^-, suggesting either a stronger lattice interaction or superior incorporation efficiency. However, when the doping level exceeded threshold concentrations, 3 mol % for SCN^- and 5 mol % for OCN^- peak splitting were observed, marking the solubility limit and the onset of phase segregation and dual-phase domains (Figure S1).

To balance phase stability with device performance, the SCN^- content was tuned from 1 to 5 mol %, revealing peak splitting beyond 3 mol %, defining the solubility limit. Even below this threshold, excess PbI_2 emerged above 1 mol %, compromising film morphology (Figure S2) and fill factor (FF) (Figure S3). Accordingly, 1 mol % SCN^- was identified as the optimal concentration for co-alloying.

The pseudohalide doping induced a non-monotonic band-gap trend, in contrast to the typical monotonic evolution in binary halide alloys. Optical absorption spectra revealed an initial small band-gap widening, peaking at 3 mol % for SCN^- and 5 mol % for OCN^-, then slightly narrowing at higher concentrations, consistent with the emergence of dual-phase domains observed by XRD (Figures 2D and S4).

Please cite this article in press as: Nandi et al., Dual-pseudohalide engineering suppresses halide segregation in wide-band-gap perovskites, Joule (2026), https://doi.org/10.1016/j.joule.2026.102669

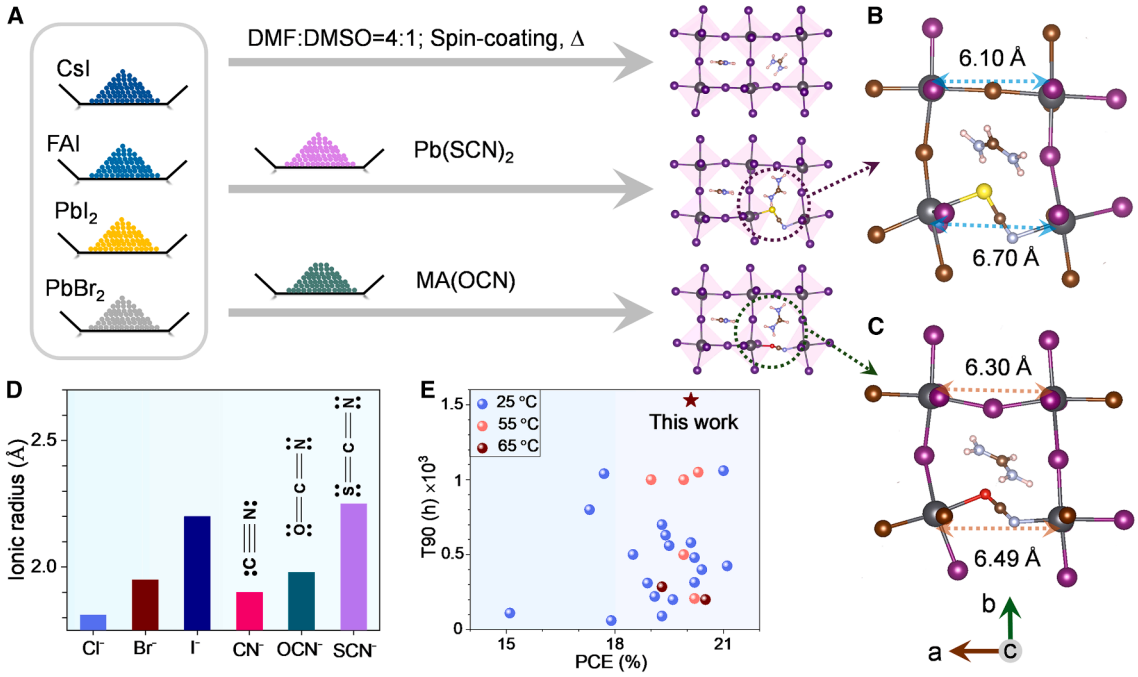

Figure 1. Formation process of SCN- and OCN-doped perovskite films

(A–C) (A) Schematic illustration of the processing pathways for ctrl, SCN^-- and OCN^--doped perovskites. *Ab initio* optimized local configurations of (B) SCN and (C) OCN within the mixed-halide perovskite lattice, highlighting their structural compatibility. Atom colors: Pb (gray), I (purple), Br (brown), N (sky blue), C (wine), S (yellow), O (red).

(D) Comparative ionic radii of relevant anions (Cl^-, Br^-, I^-, CN^-, OCN^-, and SCN^-), illustrating steric effects.

(E) Stability summary of wide-band-gap perovskites under 1-sun illumination at different temperatures: 25°C, 55°C, 65°C, and this work (star). These data and associated references are summarized in Table S1.

Exploring potential synergistic effects, SCN^- was fixed at 1 mol % (to avoid the emergence of PbI_2 as discussed), while OCN^- was varied from 1 to 5 mol %. A single-phase structure was maintained up to 3 mol % OCN^-, beyond which peak splitting and redshifted absorption indicated phase instability (Figures 2A, 2B, and S1). Based on these results, four benchmark compositions were defined for consistency and will be referred to as follows: $Cs_{0.2}FA_{0.8}Pb(I_{0.63}Br_{0.37})_3$; SCN: ctrl + 1 mol % $Pb(SCN)_2$; OCN: ctrl + 5 mol % MAOCN; dual: ctrl + 1 mol % $Pb(SCN)_2$ + 3 mol % MAOCN. Although the optimal pseudohalide incorporation level may vary with A-site composition, the cooperative lattice-distortion mechanism identified here is expected to be transferable to other FA-rich and MA-free perovskite systems.

Coupled with experimental work, ab initio calculations were performed to gain atomistic insights into the structure and energetics of pseudohalide incorporation (Figure S5). The relative formation energies for the pseudohalide ions substituting at halide sites (Figures 2C and S6–S9) indicate that OCN^- ions and dual doping are slightly more stable than SCN^- across all three compositions ($FAPbI_3$, $FAPbI_{1.75}Br_{1.25}$, and $FAPbBr_3$), confirming a higher tendency of OCN^- and dual SCN^-/OCN^- for incorporation, consistent with our experimental results. Both dopants are more stable in the mixed-halide perovskites, compared with pristine $FAPbI_3$, and show a preference for occupying Br-sites (Figure S6). The binding geometries of OCN^- and SCN^- (Figures 1B, 1C, and S5) adopt a bent, bridging configuration between adjacent Pb atoms, in which the heteroatom (O or S) coordinates to one Pb while the N atom interacts with the other. This Pb-additive-Pb linkage deviates markedly from the linear, symmetric bonding of monatomic halides in an ideal perovskite lattice and introduces pronounced local distortions.

X-Ray photoelectron spectroscopy (XPS) was employed to probe the local electronic environment around Pb^{2+} centers[36] (Figures 2E and S10). XPS analysis showed Pb 4f binding-energy shifts of 0.11 eV (SCN) and 0.32 eV (OCN) in the singly doped films. In contrast, the co-doped films exhibited a much larger 0.5 eV downshift, indicating increased electron density at Pb^{2+} sites and correspondingly weaker ligand-field interactions. This trend suggests a synergistic electronic modulation effect from co-doping, likely arising from differential coupling with the $[PbI_6]^{4-}$ octahedra.[37] Supporting this, Fourier transform infrared (FTIR) spectra revealed redshifts in the SCN^- and OCN^- stretching vibrations in dual films, compared with their singly doped counterparts (Figures 2F and S11), confirming enhanced interaction of both pseudohalides with the perovskite lattice. These effects are confirmed by the Bader charge analysis[38,39] from the density functional theory (DFT) calculations (Figure S5), showing that the charge transfer increases by 10.3% for Pb–OCN bonds and by 7.7% for Pb–SCN bonds relative to pristine $FAPbI_3$, indicating that

Please cite this article in press as: Nandi et al., Dual-pseudohalide engineering suppresses halide segregation in wide-band-gap perovskites, Joule (2026), https://doi.org/10.1016/j.joule.2026.102669

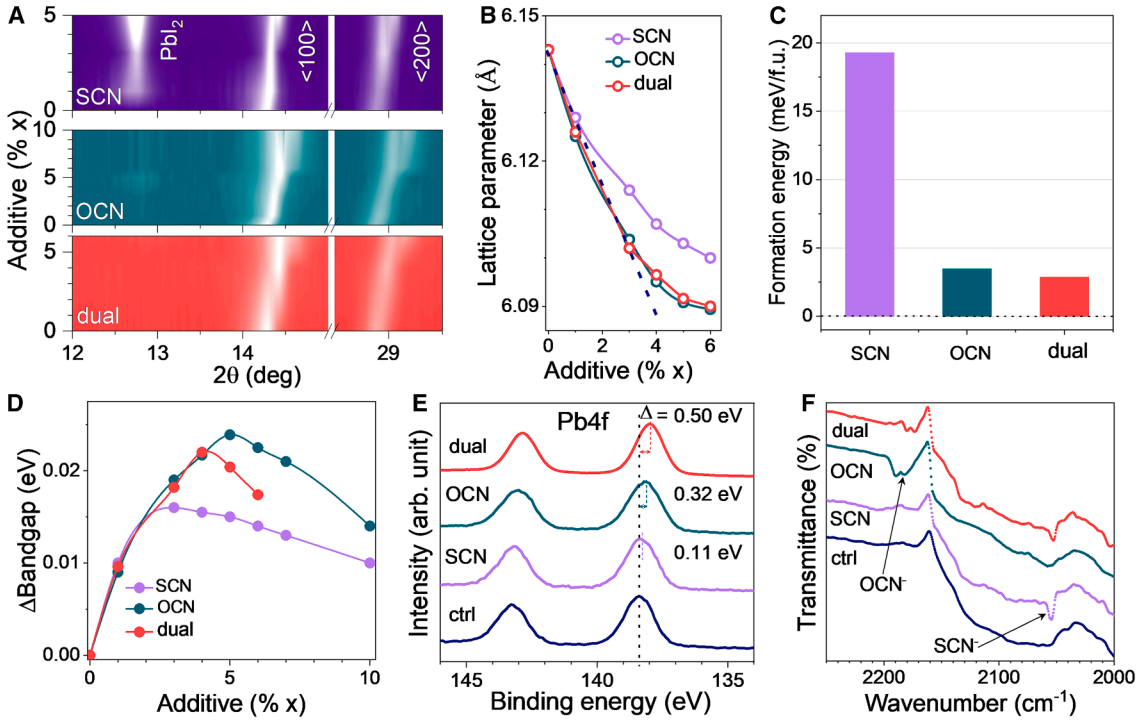

Figure 2. Structural and chemical characterization of SCN- and OCN-doped perovskite films

(A) X-ray diffraction (XRD) pattern of perovskite films doped with SCN^- (0–5 mol %), OCN^- (0–10 mol %), and dual (1 mol % SCN^- + (x − 1) mol % OCN^-) additives, highlighting the PbI_2 peak and the systematic shift in the <100> and <200> reflections. Peak bifurcation at higher additive concentrations is also highlighted here.

(B) Corresponding lattice constants calculated from (A).

(C) Formation energies of 2.47 mol % SCN^-, OCN^-, and dual-additive (SCN^- + OCN^-)-incorporated systems relative to pristine $FAPbI_3$.

(D) Relative band-gap changes (ΔE_g) with respect to ctrl, derived from Tauc plots of UV-vis spectra; dual = 1% SCN^- + (x − 1) mol % OCN^-.

(E and F) (E) Pb*4f* X-ray photoelectron spectra and (F) FTIR spectra of ctrl, SCN^-, OCN^-, and dual (1 mol % SCN^- + 3 mol % OCN^-) films, showing chemical and vibrational shifts indicative of coordination between pseudohalide anions and the perovskite lattice.

OCN^- forms a stronger interaction with Pb in accord with the XPS results.

Suppression of ion migration and halide segregation

Photostability and halide segregation in wide-band-gap perovskite films were monitored using time-dependent absorption (Figure S12) and photoluminescence (PL) (Figure S13) under continuous illumination. The ctrl film showed a gradual loss of the mixed-halide excitonic feature and emergence of iodide-rich domains, indicating LIHS.[18,19] This was quantified by the bleaching magnitude of the absorption peak (Figure S12A), with the ctrl showing the largest signal. In contrast, SCN and OCN films showed reduced bleaching, while the dual film exhibited minimal spectral change and a significant decrease in segregation rate constant (Figure S14), indicating effective suppression of halide migration. PL measurements under intense photoexcitation (10-sun equivalent, 633-nm laser) further supported this trend (Figures 3A–3C and S13). The ctrl film displayed a large redshift (~53 nm) and broadening, consistent with phase segregation. SCN and OCN films showed smaller shifts (~40 and ~22 nm, respectively), while the dual film maintained exceptional spectral stability (~5 nm shift, no broadening), confirming mitigation of LIHS.[15–17] To evaluate compositional tolerance, SCN^-/OCN^- ratios of 1:4 and 2:3 (mol %) were tested and showed improved stability over 5 mol % OCN but signs of phase heterogeneity and reduced device performance (Figures S15 and S16). Therefore, the 1:3 (mol %) SCN^-/OCN^- composition was selected for device fabrication.

The incorporation of both pseudohalides into the perovskite lattice resulted in enlarged grain sizes (Figure S17), likely owing to modified crystallization kinetics and reduced halide vacancy formation during film growth.[17,32]

Space-charge-limited current (SCLC) measurements performed on hole-only devices (Figure 3D) showed a progressive reduction in hole trap density from 2×10^{15} cm^{-3} in ctrl to 1×10^{15} cm^{-3} in SCN, 9×10^{14} cm^{-3} in OCN, and 7×10^{14} cm^{-3} in dual, as extracted from the trap-filled limit voltage (V_{TFL}) using Equation S2.[40] Consistent with this trend, the doped films exhibited lower dark current and enhanced time-resolved PL (TRPL) lifetimes, indicating reduced trap-assisted non-radiative recombination. Capacitance-voltage (C-V) measurements analyzed using the Mott-Schottky approach yielded a higher apparent built-in potential (V_{bi}) for the dual devices (1.10 V) than for the control devices (1.04 V) (Figure S18). Although the absolute values extracted from Mott-Schottky analysis in halide perovskites should be interpreted cautiously

Please cite this article in press as: Nandi et al., Dual-pseudohalide engineering suppresses halide segregation in wide-band-gap perovskites, Joule (2026), https://doi.org/10.1016/j.joule.2026.102669

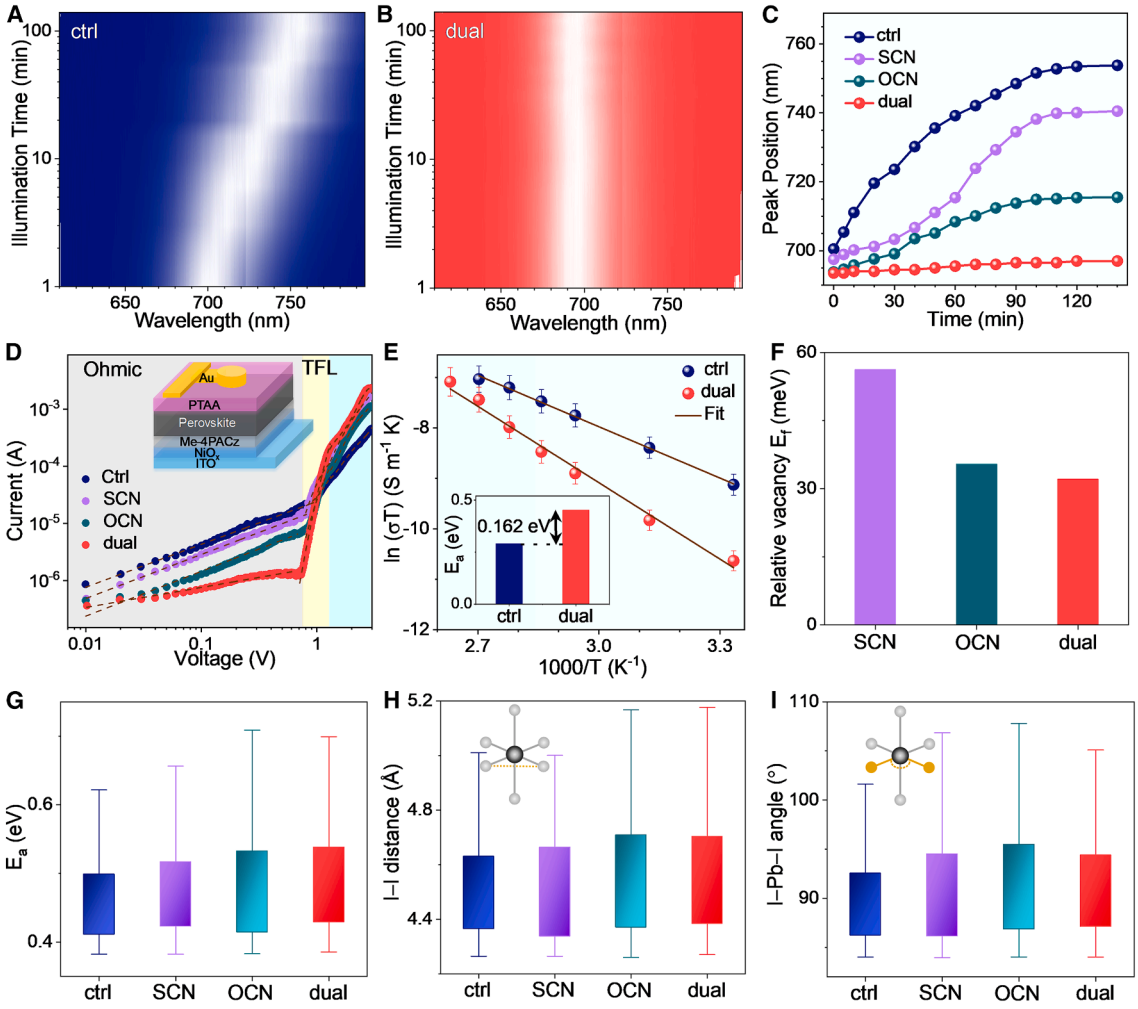

Figure 3. Mechanistic investigation of LIHS suppression via dual-pseudohalide doping

(A and B) PL spectra of ctrl and dual films under continuous 10-sun AM 1.5G illumination for 140 min, showing enhanced spectral stability in the dual system.

(C) Temporal evolution of PL spectral centroids for ctrl, SCN, OCN, and dual films, indicating the extent of halide segregation.

(D) Space-charge-limited current (SCLC) measurements of devices; inset shows the device architecture.

(E) Conductivity plots and activation energies for ion migration in ctrl and dual devices, extracted from temperature-dependent impedance spectroscopy.

(F) First-principles-calculated iodide vacancy formation energies, relative to the ctrl, for SCN^-, OCN^-, and dual-doped systems in the mixed-halide perovskite composition.

(G–I) Box-and-whisker plots of numerous local (G) iodide migration energy barriers, (H) I–I distances, and (I) I–Pb–I angles for these migration pathways derived from atomistic simulations; boxes represent interquartile ranges (middle 50% of the data), with whiskers extending from the undoped ctrl mean values (0.38 eV for migration barrier, 4.3 Å for I–I distance, and 84° for I–Pb–I angle) up to the maximum values for SCN^-, OCN^-, and dual (OCN^- + SCN^-) systems. The inset displays a schematic highlighting key structural descriptors: I–I distance and I–Pb–I angle (orange), used to assess local lattice distortion.

because of ionic contributions, the observed trend is consistent with the reduced trap density, enhanced carrier lifetimes, and increased V_{OC} of the dual devices.[41] TRPL (Figure S19) showed carrier lifetimes increasing from 16.5 ns (ctrl) to 91.9 ns (SCN), 98.4 ns (OCN), and 124.6 ns (dual), confirming reduced non-radiative recombination (Table S2). Notably, the lifetime of the control film is comparable to previously reported values (~21 ns)[2] for wide-band-gap perovskites of similar composition and band gap.

Impedance spectroscopy (Figure S20) using an equivalent circuit model[40] for mixed ionic-electronic conductors revealed increased ionic resistance (R_{ion}) upon pseudohalide doping, indicating suppressed ion migration. This was further supported by variable-temperature measurements (300–380 K), where the activation energy (E_A), extracted from Arrhenius fitting (Note S2; Equation S4), increased from 0.29 eV (ctrl) to 0.45 eV (dual) (Figures 3E and S21); this was accompanied by a notable decrease in ionic conductivity at room temperature, from 3.64×10^{-7} S m^{-1} (ctrl) to 8.05×10^{-8} S m^{-1} (dual).

The underlying atomic-scale mechanism of the observed suppression of ion migration, however, is not fully understood. Here, we extend our related ab initio simulations[41,42] to compare the local structural changes and halide vacancy formation energies for three doped systems: OCN^- alone, SCN^- alone, and dual

Please cite this article in press as: Nandi et al., Dual-pseudohalide engineering suppresses halide segregation in wide-band-gap perovskites, Joule (2026), https://doi.org/10.1016/j.joule.2026.102669

SCN^-/OCN^- (Figures 3F–3I and S22–S27). We focused on pseudohalide doping in both $FAPbI_3$ and $FAPb(I_{0.6}Br_{0.4})_3$ as this allowed us to probe trends systematically to capture effects relevant to experiments. The local structure analysis examined changes in numerous iodide–iodide (I–I) distances and I–Pb–I angles of the octahedral framework near the pseudohalide ions since they will affect iodide ion migration path lengths.

Two key features emerge. First, substantial local structural changes are found for all three cases, but the dual SCN^-/OCN^- co-doping system shows the greatest degree of local lengthening in I–I distances (up to 22% increase) and significant widening of I–Pb–I angles (up to 28% increase) for iodide migration pathways. This is consistent with the higher-activation-energy pathways observed across all additive compositions (Figure 3G), since ion migration is strongly associated with the migration jump distance between adjacent iodide sites. An example distorted pathway for the dual composition with an activation energy barrier of 0.75 eV is illustrated in Figure S27. Hence, it is the substantial local octahedral lattice distortion and steric constraints due to the dual SCN^-/OCN^- incorporation that contribute to the reduction in ion migration. Such atomic-scale mechanistic features are difficult to extract from experiments alone.

Second, such pseudohalide doping leads to higher unfavorable energies for iodide vacancy formation for all doped systems (Figures 3F, S22, and S23), leading to a quantitatively lower equilibrium population of vacancy defects. Using the Boltzmann expression for the equilibrium defect concentration, the increase in vacancy formation energy relative to the ctrl system corresponds to vacancy concentrations that are at least 3-fold lower for the mixed-halide composition at 300 K, with an even larger reduction for pristine iodide compositions (see Note S1). This substantial decrease in the vacancy population is consistent with the observed reduction in trap density. The reduced number of mobile vacancies further limits the ionic carriers available for transport, which is another contributing factor in the observed decrease in ionic conductivity.

We note that when performing the same analysis for the pure iodide system (Figures S23–S26) and where pseudohalide ions were clustered versus randomly distributed (Figure S8), the trends in energetics and structural distortions are consistent, confirming the robustness of our findings. Interestingly, the bromide vacancy formation energy across all doped compositions was consistently much higher, translating into a bromide vacancy concentration 10^5-fold lower than for iodide vacancies, validating the focus on iodide vacancy migration within the mixed-halide system. Overall, these modeling results confirm that pseudohalide co-doping effectively minimizes iodide ion migration and vacancy defect formation, contributing to enhanced device stability.

Photovoltaic devices

Following the suppression of LIHS via SCN^- and OCN^- co-doping, we fabricated wide-band-gap perovskite solar cells with the architecture ITO/NiO_x/[4-(3,6-dimethyl-9H-carbazol-9-yl)butyl]phosphonic acid (Me-4PACz)/perovskite/C60/atomic layer deposition (ALD) SnO_2/silver (Ag),[25,43] where Me-4PACz is a self-assembled monolayer. Device comparisons showed a clear power conversion efficiency (PCE) increase from ctrl to SCN/OCN, with the highest efficiency achieved in the dual device (Figure 4A), driven by enhanced V_{OC} and FF. The optimized best-performing dual device (active area 0.049 cm^2) achieved a 20.05% PCE, with V_{OC} = 1.34 V, J_{SC} = 17.83 mA cm^{-2}, and FF = 83.8% (Figure 4B), as well as a steady-state efficiency of 19.9% (Figures S28–S30).

We then investigate the long-term operating stability of encapsulated devices by maximum power point (MPP) tracking under continuous air mass 1.5 global (AM 1.5G) illumination at 65°C in an ambient atmospheric condition. The dual device shows a T90 lifetime (representing the time it takes to reach 90% of the initial PCE) of 1,530 h (Figure 4C), considerably surpassing the ctrl device, which exhibited T80 within 330 h. Notably, this stability exceeds previously reported benchmarks for wide-band-gap perovskites of a similar band gap, including T88 = 300 h at 65°C and T90 = 1,050 h at 55°C.[44,45] Dual devices also showed improved stability during ISOS-D-2 aging at 65°C in the dark, consistent with suppressed thermally activated ion migration (Figure S31). The larger gain under illumination suggests an additional reduction of photoinduced ionic redistribution and halide segregation. The beneficial effects of SCN^-/OCN^- co-alloying extend to ~2.0 eV Br-rich perovskites (Figure S32), indicating the broader applicability of this strategy to ultra wide-band-gap absorbers for triple-junction photovoltaics. The optimized wide-band-gap layer was then integrated into monolithic all-perovskite tandem solar cells, paired with a 1.26 eV narrow-band-gap $Cs_{0.05}FA_{0.7}MA_{0.25}Pb_{0.5}Sn_{0.5}I_3$ absorber (Figures S33–S35). The tandem structure (Figure 4D) achieved matched J_{SC} values of 15.8 and 16.0 mA cm^{-2} for the top and bottom cells (Figure 4F), with band gaps of 1.77 and 1.26 eV. As shown in Figures 4E–4G, the best-performing all-perovskite tandem device (active area = 0.049 cm^2) with the dual wide-band-gap subcell reached 27.2% PCE, surpassing the ctrl (25.7%), with steady-state efficiencies of 26.9% (dual) and 24.7% (ctrl) (Figure S29). Although J_{SC} and V_{OC} remain slightly below the best-reported values, these results suggest that efficiencies approaching 30% are achievable.

Long-term MPP tracking under continuous AM 1.5G illumination at 65°C in ambient air showed that the all-perovskite tandem device with the dual wide-band-gap subcell achieved a T70 lifetime of 600 h, substantially outperforming the ctrl, which reached T70 within 250 h (Figure 4H). To the best of our knowledge, this represents the longest reported MPP tracking for all-perovskite tandems under continuous illumination at 65°C (Table S1). While the narrow-band-gap Pb-Sn subcell remains a stability bottleneck, the improved durability is primarily attributed to the enhanced stability of the dual wide-band-gap layer, enabled by suppressed halide migration through increased lattice distortion and mitigation of LIHS under illumination.

Conclusions

This study addresses the persistent challenge of LIHS and ion migration in wide-band-gap perovskites that critically limits device durability and tandem integration. We introduce a dual-pseudohalide co-doping strategy in which SCN^- and

Please cite this article in press as: Nandi et al., Dual-pseudohalide engineering suppresses halide segregation in wide-band-gap perovskites, Joule (2026), https://doi.org/10.1016/j.joule.2026.102669

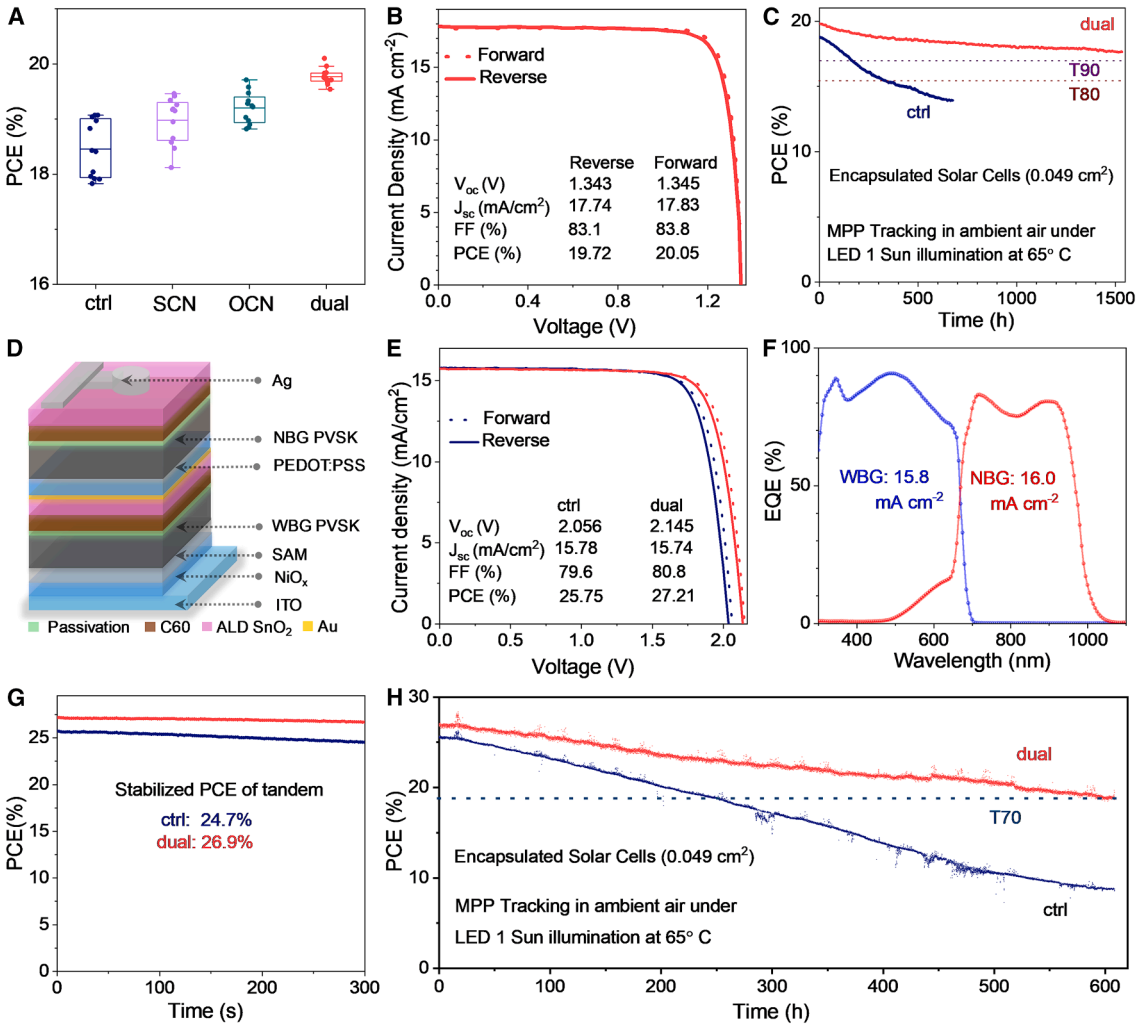

Figure 4. Device performance and stability of single-junction and tandem perovskite solar cells

(A) Efficiency statistics distribution of wide-band-gap encapsulated devices based on ctrl, SCN^-, OCN^-, and dual compositions (12 devices each).

(B) *J-V* curves of the optimized wide-band-gap dual device measured under reverse and forward scans.

(C) MPP tracking of ctrl and dual wide-band-gap encapsulated devices with area of 0.049 cm^2 measured under a white LED solar simulator with simulated 1-sun illumination at 65°C.

(D) Schematic of the monolithic all-perovskite 2T tandem device architecture.

(E) *J-V* curve of ctrl and dual tandem devices.

(F) EQE spectra of the dual tandem.

(G and H) (G) Stabilized power output of ctrl and dual tandem devices, and (H) MPP tracking results of ctrl and dual tandem devices under a white LED solar simulator with simulated 1-sun illumination at 65°C in ambient air.

OCN^- are simultaneously incorporated to engineer a synergistic lattice distortion. Unlike previous single-anion approaches, the two pseudohalides interact with Pb^{2+} through distinct coordination geometries and create an asymmetric, chemically frustrated sublattice. This cooperative distortion raises halide vacancy formation energies, perturbs I-I jump pathways, and increases ion migration barriers, which cumulatively suppress LIHS by nearly an order of magnitude. The resulting quadruple-anion framework yields films of superior structural and optoelectronic stability, enabling wide-band-gap devices with 20.05% efficiency that retain 90% of their initial PCE after 1,530 h of continuous illumination at 65°C. When integrated into all-perovskite tandems, the stabilized absorber delivers 27.2% efficiency with excellent thermal endurance. These findings establish dual-pseudohalide alloying as a fundamentally new materials-design principle for durable, high-performance all-perovskite tandem photovoltaics.

METHODS

Materials

All materials were used as received without further purification. Commercial ITO substrates (20 Ω per square, 25 × 25 mm^2) were purchased from TFD. Organic halide salts (FAI, FABr, MAI) and 4-fluorophenethylammonium bromide (4F-PEABr)

Please cite this article in press as: Nandi et al., Dual-pseudohalide engineering suppresses halide segregation in wide-band-gap perovskites, Joule (2026), https://doi.org/10.1016/j.joule.2026.102669

were purchased from GreatCell Solar Materials. PEDOT:PSS aqueous solution (no. AI 4083) was purchased from Heraeus Clevios. PbI_2 (99.99%), $PbBr_2$ (99.999%), CsI (over 99.0%), CsBr (over 99.0%), and Me-4PACz were purchased from TCI Chemicals. SnI_2 (99.99%), SnF_2 (99%), glycine hydrochloride (99%), guanidine thiocyanate (GuaSCN, 99%), and ethane-1,2-diammonium iodide ($EDAI_2$, 98%) were purchased from Sigma-Aldrich. C60, bathocuproine (BCP), and $PDAI_2$ were purchased from Xi'an Polymer Light Technology. All solvents used in the process were anhydrous and purchased from Sigma-Aldrich.

Perovskite precursor solutions

Wide-band-gap perovskite

To prepare the wide-band-gap perovskite precursor solution (1.15 M, $FA_{0.8}Cs_{0.2}Pb(I_{0.6}Br_{0.4})_3$), stoichiometric amounts of CsI, FAI, $PbBr_2$, and PbI_2 were dissolved in a solvent blend of dimethylformamide (DMF) and dimethyl sulfoxide (DMSO) mixed at a 4:1 volume ratio. The solution was stirred at 60°C for 1 h and subsequently filtered through a 0.22-μm polytetrafluoroethylene (PTFE) membrane filter.

Narrow-band-gap perovskite

A narrow-band-gap perovskite precursor solution (1.8 M, $Cs_{0.05}FA_{0.7}MA_{0.25}Pb_{0.5}Sn_{0.5}I_3$) was prepared by dissolving CsI, FAI, MAI, SnI_2, and PbI_2 in a 3:1 (v/v) mixture of DMF and DMSO. Additives, including tin powder (5 mg), GuaSCN (4 mg), SnF_2 (14 mg), 4F-PEABr (2 mg), and glycine hydrochloride (4 mg), were subsequently introduced. The solution was stirred for 1 h at room temperature and filtered through a 0.22-μm PTFE membrane before use.

Solar cell fabrication

Single-junction wide-band-gap perovskite solar cells

ITO-coated glass substrates were sequentially cleaned in a laboratory-grade detergent solution, deionized (DI) water, isopropanol (IPA), and acetone, with each cleaning step conducted for 15 min in an ultrasonic bath. Following the cleaning process, the substrates were dried under a nitrogen (N_2) stream and subjected to a 30-min UV-ozone treatment to enhance surface wettability and remove residual organic contaminants.

For the hole transport layer (HTL), a NiOx nanoparticle dispersion (Avantama) in ethanol was diluted at a 1:9 volume ratio and spin-coated onto the cleaned ITO substrates at 4,000 rpm for 25 s in ambient conditions. No post-deposition annealing was applied. Immediately after deposition, the substrates were transferred to an N_2-filled glovebox.

A self-assembled monolayer of Me-4PACz (0.3 mg/mL in ethanol) was subsequently deposited onto the NiOx layer by spin-coating at 4,000 rpm for 25 s, followed by thermal annealing at 100°C for 10 min.

For perovskite film fabrication, the precursor solution was deposited onto the substrate, which was then spin-coated at 4,000 rpm for 32 s with an acceleration of 1,000 rpm/s. During the final 8 s of spinning, 150 μL of anisole was dispensed as an antisolvent to induce crystallization. The resulting film was annealed at 100°C for 15 min on a hotplate.

Organic surface passivation solutions were prepared by dissolving $EDAI_2$ and phenylethylammonium iodide (PEAI) in IPA at varying concentrations. For the passivation step, a solution containing 0.5 mg $EDAI_2$ and 1 mg PEAI in 1 mL IPA was spin-coated onto the perovskite layer at 4,000 rpm for 25 s with an acceleration of 1,000 rpm/s. The film was then thermally annealed at 100°C for 5 min to complete the treatment.

After cooling to room temperature, the substrates were transferred to a vacuum evaporation system for deposition of a 27-nm-thick C60 electron transport layer via thermal evaporation at a rate of 0.2 Å/s. Next, ALD was performed to deposit a 15-nm SnO_2 layer at 90°C using tetrakis(dimethylamino)tin(IV) (99.9999% purity) and DI water as precursors in a Savannah ALD system. The Sn precursor was pulsed for 0.5 s and purged for 15 s, while DI water was pulsed for 15 ms and purged for 15 s, both under a constant 20 sccm N_2 flow. Finally, a 140-nm Ag electrode was deposited via thermal evaporation at a deposition rate of 1 Å/s to complete the device structure.

All-perovskite tandem solar cells

Fabrication of the wide-band-gap perovskite solar cell proceeded as previously described up to the deposition of the SnO_2 electron transport layer via ALD. Following the SnO_2 deposition, a 1-nm gold (Au) interconnection layer was thermally evaporated onto the surface.

Subsequently, a layer of PEDOT:PSS (diluted in IPA at a 1:2 volume ratio) was spin-coated onto the wide-band-gap subcell at 4,000 rpm for 30 s and annealed at 120°C for 10 min under ambient conditions. Once cooled, the substrates were transferred to an N_2-filled glovebox to enable fabrication of the narrow-band-gap perovskite subcell. The narrow-band-gap perovskite precursor solution was deposited in a two-step spin-coating process: first at 1,000 rpm for 10 s, followed by 3,800 rpm for 45 s. During the second step, 400 μL of toluene was dynamically dispensed onto the spinning substrate 20 s before completion to facilitate antisolvent-assisted crystallization. The resulting film was annealed at 100°C for 10 min. Post-deposition surface treatment was performed using $EDAI_2$. A 0.5 mg/mL solution of $EDAI_2$ in a 4:3 (v/v) mixture of IPA and toluene was spin-coated at 4,000 rpm for 25 s, followed by a 5-min annealing step at 100°C.

To complete the device, subsequent layers, C60 (27 nm), ALD-deposited SnO_2 (15 nm), and thermally evaporated Ag (140 nm), were sequentially deposited using the same conditions as previously described.

Device testing

Current density-voltage (*J-V*) measurements were conducted using a Keithley 2450 source meter under simulated AM 1.5G solar illumination provided by a Class A solar simulator (Newport). The light intensity was calibrated to 100 mW cm^{-2} using a certified reference cell (Newport 91150V). *J-V* curves were acquired in an N_2-filled atmosphere at a scan rate of 100 mV s^{-1}, with a voltage step size of 10 mV and a delay time of 200 ms. The active area was determined by the aperture shade mask (0.049 cm^2 for small-area devices) placed in front of the solar cell.

External quantum efficiency (EQE) spectra were recorded in ambient conditions using a QuantX-300 Quantum Efficiency Measurement System (Newport). Monochromatic light was focused onto the active pixel of the device, with a chopper frequency of 20 Hz employed for signal modulation. For tandem solar cell characterization, EQE measurements were carried out

Please cite this article in press as: Nandi et al., Dual-pseudohalide engineering suppresses halide segregation in wide-band-gap perovskites, Joule (2026), https://doi.org/10.1016/j.joule.2026.102669

under ambient conditions using bias illumination from high-intensity LEDs. Specifically, 850- and 450-nm LEDs were employed to isolate and characterize the rear and front subcells, respectively. No external bias voltage was applied during EQE acquisition for tandem devices to ensure unperturbed spectral response.

Stability testing

Device stability was monitored using a custom-built stability tracking system. Both single-junction and tandem perovskite solar cells were illuminated with a white light LED source, calibrated to deliver an intensity equivalent to AM 1.5G 1-sun conditions. During testing, devices were placed on a temperature-controlled hotplate maintained at 65°C to simulate accelerated aging conditions. Encapsulation was carried out using a glass capping system, sealed with UV-curable adhesive (Lumtec LT-U001) to prevent moisture and oxygen ingress. For MPP tracking, measurements were conducted under ambient atmosphere in the testing chamber. The operating voltage corresponding to MPP was determined from forward and reverse *J-V* scans prior to stabilization. Devices were then biased at this fixed voltage, and the output current was recorded at 2-min intervals to evaluate operational stability over time.

Characterization

XRD patterns were recorded using a Rigaku Miniflex600 diffractometer equipped with D/tex detector and an Ni-filtered Cu Kα radiation source. Ultraviolet-visible (UV-vis) transmittance spectra were measured using a Cary 5000 UV-vis-NIR spectrophotometer operating in the 300- to 800-nm region at room temperature. Halide segregation studies were conducted under white light LED illumination, calibrated to simulate AM 1.5G 1-sun conditions. Steady-state PL spectra were acquired with a Horiba LabRAM HR Evolution confocal Raman microscope, using a 473-nm laser for excitation, a 5× objective lens, and a neutral density (ND) filter (transmission: 0.01%). The laser power density at the sample surface was estimated to be ~1,000 mW/cm^2. Scanning electron microscopy (SEM) images were obtained using the Hitachi S8030 microscope operated at an accelerating voltage of 3 kV. The XPS instrument was calibrated using Ag metal, setting the Ag 3d5/2 peak at 368.2 eV. A low-energy electron gun was used throughout to neutralize surface charge. In post-processing, the adventitious carbon peak at 284.8 eV was used to calibrate spectra and mitigate charging effects. Each sample was grounded using copper conductive tape, and charge compensation was performed before each measurement. Nyquist plots were measured using a Solartron 1260A frequency response analyzer, and ionic resistance was extracted from the plot using equivalent circuit fitting to determine the ionic conductivity σ. The activation energy E_A was obtained from variable-temperature ionic conductivity measurements and determined using an Arrhenius plot of log(σ × T) and inverse of temperature (1,000/T). SCLC measurements were conducted by measuring the dark I-V characteristics of hole-only devices with the structure ITO/NiO_x/self-assembled monolayer (SAM)/perovskite/PTAA/Au using a Keithley 2410 high-voltage source meter and a Keithley 6517 electrometer. C-V measurements were conducted using a Wayne Kerr 6440B LCR meter integrated with a SemiProbe PS4L automatic probe station. The measurements were carried out in the dark using an AC perturbation amplitude of 50 mV over a frequency range of 20 Hz–1 MHz. The V_{bi} was extracted from the intercept of the linear region of the Mott-Schottky plots according to Equation S3. TRPL measurements were performed using an FL920 spectrometer (Edinburgh Instruments) operating in the time-correlated single-photon counting (TCSPC) mode. Thin films of perovskite samples were excited with a pulsed 375-nm diode laser, and the PL decay was recorded by accumulating photon arrival events relative to the excitation pulse. The resulting decay profiles were analyzed to extract the carrier lifetimes.

Computational modeling

First-principles calculations were performed using DFT in Vienna ab initio simulation package (VASP) 6.4.1 with the projector augmented-wave (PAW) method and Perdew-Burke-Ernzerhof (PBE)-generalized gradient approximation (GGA) exchange-correlation functional. DFT-D3 dispersion correction was included to account for van der Waals interactions. A plane-wave cutoff of 500 eV and Γ-centered k-point meshes (spacing 0.20–0.15 Å^{-1}) were employed. All structures were fully relaxed until forces were <0.01 eV Å^{-1} and electronic energies converged to 10^{-6} eV. Iodide migration barriers were obtained with the climbing-image nudged elastic band (CI-NEB) method, accelerated by a machine-learned interatomic potential trained on r^{2}SCAN reference data. Further details of computational modeling are given in Note S1.

RESOURCE AVAILABILITY

Lead contact

Requests for further information, resources, and materials should be directed to, and will be fulfilled by, the lead contact, Mercouri G. Kanatzidis (m-kanatzidis@northwestern.edu).

Materials availability

All materials generated in this study are available from the lead contact with reasonable requirements.

Data and code availability

All data and code supporting this study are publicly available in the GitHub repository dual_pseudohalide_additives (https://github.com/vikram89v/dual_pseudohalide_additives), archived at Zenodo: https://doi.org/10.5281/zenodo.21733656. The archive contains the source data plotted in Figures 1, 2, 3, and 4, the DFT-optimized structures and VASP input parameters, the structure sets used for training, and the message passing atomic cluster expansion (MACE) foundation model, fine-tuned model, and training parameters. Additional data supporting the findings of this study are available from the corresponding authors upon reasonable request.

ACKNOWLEDGMENTS

This work made use of the IMSERC (RRID:SCR_017874), Keck-II (RRID: SCR_026360), EPIC (RRID: SCR_026361), and NUFAB (RRID: SCR_017779) physical characterization facility at Northwestern University, which has received support from the SHyNE Resource (NSF ECCS-2025633), the IIN, and Northwestern's MRSEC program (NSF DMR-2308691). This work was supported by the Paula M. Trienens Institute for Sustainability and Energy at Northwestern University. Research reported in this publication was supported in part by instrumentation provided by the NSF (award DMR-2117727). L.H., S.S.H., and M.C.H. acknowledge support from the National Science Foundation (NSF) Assessing and Predicting Technology Outcomes (APTO) Program (grant no. TF-2404035). M.S.I. and V. acknowledge the Engineering and Physical Sciences Research Council (EPSRC) Programme Grant (EP/X038777/1) for a

postdoctoral fellowship and are grateful to the UK's HEC Materials Chemistry Consortium (EP/X035859/1) for ARCHER2 supercomputing resources. A.J. gratefully acknowledges support from The Attisani Scholarship in Zero Carbon Energy Research (ZERO Institute, University of Oxford), funded by the Ezgi And Michele Attisani Family Foundation.

AUTHOR CONTRIBUTIONS

P.N. conceived the idea and designed the project. P.N. fabricated, tested, and characterized the films and solar cells. C.-H.C. and Y.W. assisted with device fabrication and characterization. L.H. and S.S.H. performed capacitance-voltage (C-V) measurements and analysis under the supervision of M.C.H. V. and A.J. performed first-principles DFT calculations and MD simulations and analyzed the computational results under the supervision of M.S.I. P.N. wrote the manuscript, with contributions from C.L., V., B.C., M.S.I., and M.G.K. to its reviewing and editing. E.H.S. and M.G.K. supervised the work. All authors discussed the results and commented on the manuscript.

DECLARATION OF INTERESTS

P.N., B.C., E.H.S., and M.G.K. filed a patent related to this work.

SUPPLEMENTAL INFORMATION

Supplemental information can be found online at https://doi.org/10.1016/j.joule.2026.102669.

Received: February 11, 2026
Revised: June 16, 2026
Accepted: August 11, 2026

REFERENCES

1. Wen, J., Hu, H., Chen, C., McMeekin, D.P., Xiao, K., Lin, R., Liu, Y., Snaith, H.J., Tang, J., Paetzold, U.W., et al. (2025). Present status of and future opportunities for all-perovskite tandem photovoltaics. Nat. Energy *10*, 681–696. https://doi.org/10.1038/s41560-025-01782-0.
2. Liu, Z., Lin, R., Wei, M., Yin, M., Wu, P., Li, M., Li, L., Wang, Y., Chen, G., Carnevali, V., et al. (2025). All-perovskite tandem solar cells achieving >29% efficiency with improved (100) orientation in wide-bandgap perovskites. Nat. Mater. *24*, 252–259. https://doi.org/10.1038/s41563-024-02073-x.
3. Renshuo Solar (2024) . All-perovskite tandem cells reach a certified efficiency of up to 30.1%. https://mp.weixin.qq.com/s/3Ggl6caaTiTABNq0sFcbQ.
4. Duan, C., Zhang, K., Peng, Z., Li, S., Zou, F., Wang, F., Li, J., Zhang, Z., Chen, C., Zhu, Q., et al. (2025). Durable all-inorganic perovskite tandem photovoltaics. Nature *637*, 1111–1117. https://doi.org/10.1038/s41586-024-08432-7.
5. Yao, Y., Liu, S., Rodríguez-Gallegos, C.D., Rodríguez-Gallegos, C.A., Wang, Z., and Hou, Y. (2025). Perovskite-based multi-junction solar cells. Nat. Rev. Clean Technol. *1*, 771–787. https://doi.org/10.1038/s44359-025-00103-8.
6. Hu, S., Wang, J., Zhao, P., Pascual, J., Wang, J., Rombach, F., Dasgupta, A., Liu, W., Truong, M.A., Zhu, H., et al. (2025). Steering perovskite precursor solutions for multijunction photovoltaics. Nature *639*, 93–101. https://doi.org/10.1038/s41586-024-08546-y.
7. Xiao, Z., Yuan, Y., Shao, Y., Wang, Q., Dong, Q., Bi, C., Sharma, P., Gruverman, A., and Huang, J. (2015). Giant switchable photovoltaic effect in organometal trihalide perovskite devices. Nat. Mater. *14*, 193–198. https://doi.org/10.1038/nmat4150.
8. Kim, T., Park, S., Iyer, V., Shaheen, B., Choudhry, U., Jiang, Q., Eichman, G., Gnabasik, R., Kelley, K., Lawrie, B., et al. (2023). Mapping the pathways of photo-induced ion migration in organic-inorganic hybrid halide perovskites. Nat. Commun. *14*, 1846. https://doi.org/10.1038/s41467-023-37486-w.
9. Thiesbrummel, J., Milić, J.V., Deibel, C., Garnett, E.C., Tao, S., Kirchartz, T., Guerrero, A., Cameron, P., Tress, W., Islam, M.S., et al. (2026). Ion migration in perovskite solar cells. Nat. Rev. Chem. *10*, 179–195. https://doi.org/10.1038/s41570-025-00790-8.
10. Hoke, E.T., Slotcavage, D.J., Dohner, E.R., Bowring, A.R., Karunadasa, H.I., and McGehee, M.D. (2015). Reversible photo-induced trap formation in mixed-halide hybrid perovskites for photovoltaics. Chem. Sci. *6*, 613–617. https://doi.org/10.1039/C4SC03141E.
11. Slotcavage, D.J., Karunadasa, H.I., and McGehee, M.D. (2016). Light-Induced Phase Segregation in Halide-Perovskite Absorbers. ACS Energy Lett. *1*, 1199–1205. https://doi.org/10.1021/acsenergylett.6b00495.
12. Nandi, P., Giri, C., Swain, D., Manju, U., Mahanti, S.D., and Topwal, D. (2018). Temperature Dependent Photoinduced Reversible Phase Separation in Mixed-Halide Perovskite. ACS Appl. Energy Mater. *1*, 3807–3814. https://doi.org/10.1021/acsaem.8b00587.
13. McMeekin, D.P., Sadoughi, G., Rehman, W., Eperon, G.E., Saliba, M., Hörantner, M.T., Haghighirad, A., Sakai, N., Korte, L., Rech, B., et al. (2016). A mixed-cation lead mixed-halide perovskite absorber for tandem solar cells. Science *351*, 151–155. https://doi.org/10.1126/science.aad5845.
14. Mao, W., Hall, C.R., Bernardi, S., Cheng, Y.-B., Widmer-Cooper, A., Smith, T.A., and Bach, U. (2021). Light-induced reversal of ion segregation in mixed-halide perovskites. Nat. Mater. *20*, 55–61. https://doi.org/10.1038/s41563-020-00826-y.
15. Xu, J., Boyd, C.C., Yu, Z.J., Palmstrom, A.F., Witter, D.J., Larson, B.W., France, R.M., Werner, J., Harvey, S.P., Wolf, E.J., et al. (2020). Triple-halide wide–band gap perovskites with suppressed phase segregation for efficient tandems. Science *367*, 1097–1104. https://doi.org/10.1126/science.aaz5074.
16. Wang, Z., Zeng, L., Zhu, T., Chen, H., Chen, B., Kubicki, D.J., Balvanz, A., Li, C., Maxwell, A., Ugur, E., et al. (2023). Suppressed phase segregation for triple-junction perovskite solar cells. Nature *618*, 74–79. https://doi.org/10.1038/s41586-023-06006-7.
17. Zhang, Z., Chen, W., Jiang, X., Cao, J., Yang, H., Chen, H., Yang, F., Shen, Y., Yang, H., Cheng, Q., et al. (2024). Suppression of phase segregation in wide-bandgap perovskites with thiocyanate ions for perovskite/organic tandems with 25.06% efficiency. Nat. Energy *9*, 592–601. https://doi.org/10.1038/s41560-024-01491-0.
18. Nandi, P., Li, Z., Kim, Y., Ahn, T.K., Park, N.-G., and Shin, H. (2021). Stabilizing Mixed Halide Lead Perovskites against Photoinduced Phase Segregation by A-Site Cation Alloying. ACS Energy Lett. *6*, 837–847. https://doi.org/10.1021/acsenergylett.0c02631.
19. Elmelund, T., Seger, B., Kuno, M., and Kamat, P.V. (2020). How Interplay between Photo and Thermal Activation Dictates Halide Ion Segregation in Mixed Halide Perovskites. ACS Energy Lett. *5*, 56–63. https://doi.org/10.1021/acsenergylett.9b02265.
20. Brivio, F., Caetano, C., and Walsh, A. (2016). Thermodynamic Origin of Photoinstability in the CH3NH3Pb(I1–xBrx)3 Hybrid Halide Perovskite Alloy. J. Phys. Chem. Lett. *7*, 1083–1087. https://doi.org/10.1021/acs.jpclett.6b00226.
21. Bischak, C.G., Hetherington, C.L., Wu, H., Aloni, S., Ogletree, D.F., Limmer, D.T., and Ginsberg, N.S. (2017). Origin of Reversible Photoinduced Phase Separation in Hybrid Perovskites. Nano Lett. *17*, 1028–1033. https://doi.org/10.1021/acs.nanolett.6b04453.
22. Barker, A.J., Sadhanala, A., Deschler, F., Gandini, M., Senanayak, S.P., Pearce, P.M., Mosconi, E., Pearson, A.J., Wu, Y., Srimath Kandada, A.R., et al. (2017). Defect-Assisted Photoinduced Halide Segregation in Mixed-Halide Perovskite Thin Films. ACS Energy Lett. *2*, 1416–1424. https://doi.org/10.1021/acsenergylett.7b00282.
23. Xu, N., Qi, X., Shen, Z., Hu, L., Lv, J., Zhong, Y., Wang, B., and Zou, Z. (2025). Point defects in metal halide perovskites. Nat. Rev. Phys. *7*, 554–564. https://doi.org/10.1038/s42254-025-00861-1.

24. Yuan, Y., and Huang, J. (2016). Ion Migration in Organometal Trihalide Perovskite and Its Impact on Photovoltaic Efficiency and Stability. Acc. Chem. Res. *49*, 286–293. https://doi.org/10.1021/acs.accounts.5b00420.

25. Chen, H., Maxwell, A., Li, C., Teale, S., Chen, B., Zhu, T., Ugur, E., Harrison, G., Grater, L., Wang, J., et al. (2023). Regulating surface potential maximizes voltage in all-perovskite tandems. Nature *613*, 676–681. https://doi.org/10.1038/s41586-022-05541-z.

26. Knight, A.J., and Herz, L.M. (2020). Preventing phase segregation in mixed-halide perovskites: a perspective. Energy Environ. Sci. *13*, 2024–2046. https://doi.org/10.1039/D0EE00788A.

27. Cho, J., and Kamat, P.V. (2020). How Chloride Suppresses Photoinduced Phase Segregation in Mixed Halide Perovskites. Chem. Mater. *32*, 6206–6212. https://doi.org/10.1021/acs.chemmater.0c02100.

28. He, X.-Y., Song, B., Wang, K.-L., Li, N., Huang, L., Qin, R.-H., Chen, J., Chen, C.-H., Xia, Y., Yavuz, I., et al. (2025). Stopping Phase Separation Enables Durable Wide-Bandgap Photovoltaic Perovskites. Adv. Mater. *38*, e18492. https://doi.org/10.1002/adma.202518492.

29. Chang, Q., Yun, Y., Cao, K., Yao, W., Huang, X., He, P., Shen, Y., Zhao, Z., Chen, M., Li, C., et al. (2024). Highly Efficient and Stable Perovskite Solar Modules Based on FcPF6 Engineered Spiro-OMeTAD Hole Transporting Layer. Adv. Mater. *36*, e2406296. https://doi.org/10.1002/adma.202406296.

30. Nandi, P., Park, H., Shin, S., Sharbirin, A.S., Kim, J., Kwon, S.J., Park, N.-G., and Shin, H. (2023). Superhalogen modulation: an effective approach for minimizing light-induced halide segregation in $MAPb(I_{0.7}Br_{0.3})_3$. J. Mater. Chem. A *11*, 19004–19016. https://doi.org/10.1039/D3TA04201D.

31. Sanchez-Diaz, J., Sánchez, R.S., Masi, S., Krečmarová, M., Alvarez, A.O., Barea, E.M., Rodriguez-Romero, J., Chirvony, V.S., Sánchez-Royo, J.F., Martinez-Pastor, J.P., et al. (2022). Tin perovskite solar cells with >1,300h of operational stability in N_2 through a synergistic chemical engineering approach. Joule *6*, 861–883. https://doi.org/10.1016/j.joule.2022.02.014.

32. Liu, S., Lu, Y., Yu, C., Li, J., Luo, R., Guo, R., Liang, H., Jia, X., Guo, X., Wang, Y.-D., et al. (2024). Triple-junction solar cells with cyanate in ultra-wide-bandgap perovskites. Nature *628*, 306–312. https://doi.org/10.1038/s41586-024-07226-1.

33. Matheu, R., Vigil, J.A., Crace, E.J., and Karunadasa, H.I. (2022). The halogen chemistry of halide perovskites. Trends Chem. *4*, 206–219. https://doi.org/10.1016/j.trechm.2021.12.002.

34. Dang, H.X., Wang, K., Ghasemi, M., Tang, M.-C., De Bastiani, M., Aydin, E., Dauzon, E., Barrit, D., Peng, J., Smilgies, D.-M., et al. (2019). Multication Synergy Suppresses Phase Segregation in Mixed-Halide Perovskites. Joule *3*, 1746–1764. https://doi.org/10.1016/j.joule.2019.05.016.

35. Lin, P.-Y., Lin, C.-F., Chiu, Y.-Y., Chen, H.-H., Li, M.-H., Raja, R., Wu, C.-S., Hou, C.-H., Sung-Yun Hsiao, S., Shyue, J.-J., et al. (2023). Revealing the Role of Thiocyanate for Improving the Performance of Perovskite Solar Cells. ACS Appl. Energy Mater. *6*, 79–88. https://doi.org/10.1021/acsaem.2c02291.

36. Liu, C., Yang, Y., Chen, H., Spanopoulos, I., Bati, A.S.R., Gilley, I.W., Chen, J., Maxwell, A., Vishal, B., Reynolds, R.P., et al. (2024). Two-dimensional perovskitoids enhance stability in perovskite solar cells. Nature *633*, 359–364. https://doi.org/10.1038/s41586-024-07764-8.

37. De Keersmaecker, M., Dietrich, P., Bahri, M., Browning, N.D., Armstrong, N.R., and Ratcliff, E.L. (2025). Activated Corrosion and Recovery in Lead Mixed-Halide Perovskites Revealed by Dynamic Near-Ambient Pressure X-ray Photoelectron Spectroscopy. J. Am. Chem. Soc. *147*, 8881–8892. https://doi.org/10.1021/jacs.5c00668.

38. Tang, W., Sanville, E., and Henkelman, G. (2009). A grid-based Bader analysis algorithm without lattice bias. J. Phys. Condens. Matter *21*, 084204. https://doi.org/10.1088/0953-8984/21/8/084204.

39. Yu, M., and Trinkle, D.R. (2011). Accurate and efficient algorithm for Bader charge integration. J. Chem. Phys. *134*, 064111. https://doi.org/10.1063/1.3553716.

40. Senocrate, A., Moudrakovski, I., Kim, G.Y., Yang, T.-Y., Gregori, G., Grätzel, M., and Maier, J. (2017). The Nature of Ion Conduction in Methylammonium Lead Iodide: A Multimethod Approach. Angew. Chem. Int. Ed. *56*, 7755–7759. https://doi.org/10.1002/anie.201701724.

41. Ferdani, D.W., Pering, S.R., Ghosh, D., Kubiak, P., Walker, A.B., Lewis, S.E., Johnson, A.L., Baker, P.J., Islam, M.S., and Cameron, P.J. (2019). Partial cation substitution reduces iodide ion transport in lead iodide perovskite solar cells. Energy Environ. Sci. *12*, 2264–2272. https://doi.org/10.1039/C9EE00476A.

42. Lin, Y.-H., Vikram, Yang, F., Cao, X.-L., Dasgupta, A., Oliver, R.D.J., Ulatowski, A.M., McCarthy, M.M., Shen, X., Yuan, Q., et al. (2024). Bandgap-universal passivation enables stable perovskite solar cells with low photovoltage loss. Science *384*, 767–775. https://doi.org/10.1126/science.ado2302.

43. Choi, D., Shin, D., Li, C., Liu, Y., Bati, A.S.R., Kachman, D.E., Yang, Y., Li, J., Lee, Y.J., Li, M., et al. (2025). Carboxyl-functionalized perovskite enables ALD growth of a compact and uniform ion migration barrier. Joule *9*, 101801. https://doi.org/10.1016/j.joule.2024.12.002.

44. Wu, Z., Zhao, Y., Wang, C., Ma, T., Chen, C., Liu, Y., Jia, T., Zhai, Y., Chen, C., Zhang, C., et al. (2025). Enhancing Photovoltaically Preferred Orientation in Wide-Bandgap Perovskite for Efficient All-Perovskite Tandem Solar Cells. Adv. Mater. *37*, e2412943. https://doi.org/10.1002/adma.202412943.

45. Fu, S., Zhou, S., Meng, W., Li, G., Dong, K., Pu, D., Zhou, J., Wang, C., Guan, H., Shao, W., et al. (2025). Piracetam shapes wide-bandgap perovskite crystals for scalable perovskite tandems. Nat. Nanotechnol. *20*, 764–771. https://doi.org/10.1038/s41565-025-01899-z.